Ionospheric Variability Effects on Impulsive ELF Antipodal Propagation About the Earth Sphere

Bach T. Nguyen, Stephen E. Wiechecki Vergara, *Member, IEEE*, Costas D. Sarris, *Senior Member, IEEE*, and Jamesina J. Simpson, *Senior Member, IEEE*

Abstract—Analytical and numerical solutions to extremely low-frequency electromagnetic wave propagation in the earth–ionosphere waveguide nearly always assume average (mean) material properties at each position of interest and only solve for the average (mean) electric and magnetic fields. However, numerically assuming only an average state of the ionosphere yields calculated output electromagnetic field waveforms that are not as rich and complex as measured electromagnetic fields. Furthermore, there is great uncertainty in the content of the ionosphere at any given moment. In this paper, global stochastic finite-difference time-domain models of the earth–ionosphere waveguide are generated for the first time. These models use the Galerkin-based polynomial chaos expansion method to efficiently calculate both the mean and variance of the electric and magnetic fields due to uncertainties and variances in the state of the ionosphere. The proposed method is validated through comparisons with brute-force Monte Carlo results.

Index Terms—Earth–ionosphere cavity, electromagnetic wave propagation, finite-difference time-domain (FDTD), ionospheric conductivity, polynomial chaos, uncertainty.

I. INTRODUCTION

THE ionosphere and Earth's ground form a spherical annular cavity in which extremely low-frequency (ELF: 3 Hz–3 kHz) electromagnetic waves propagate on a global scale. Accurate models of the ELF wave propagation in the earth–ionosphere waveguide are helpful for studying lightning and sprites, global temperature change, hypothesized earthquake precursors, remote sensing, and communications, as well as other geophysical phenomena and engineering applications [1]–[4].

Analytical and numerical models have been developed to study the ELF propagation. Most analytical approaches are based on ray theory for short-distant propagation and mode theory for long-distant propagation (e.g., [5]–[7]).

Alternatively, the transmission line method has been used (e.g., [8], [9]). In general, analytical methods are very fast and computationally efficient; however, they can only provide solutions for specific scenarios wherein simplifying assumptions have been made (such as ignoring much of the Earth's topographical details and ionospheric inhomogeneity). More recently, numerical methods have been developed to take advantage of modern supercomputing capabilities via a high-resolution spatial mesh of grid cells that may be assigned to the varying electrical details of the lithosphere, ionosphere, and oceans. The finite-difference time-domain (FDTD) method [10] is particularly attractive for this problem [11]–[18].

The analytical and numerical solutions to the ELF electromagnetic wave propagation in the earth–ionosphere waveguide at frequencies of less than 3 kHz nearly always assume average (mean) material properties at each position of interest and only solve for the average (mean) electric and magnetic fields. References [19], [20], and [21] were developed to account for the uncertainty of the ionosphere on electromagnetic wave propagation; however, these are implemented in a Cartesian grid of homogeneous magnetized ionospheric plasma.

The continual fluctuation of the state of the ionosphere has resulted in the generation of many different ionosphere conductivity models over time [22]–[26]. Three observations may be made about these various conductivity models.

1) There are notable differences between these models because different methodologies and approaches are used to generate them.
2) These models cannot be adequately verified because there is little experimental data on the ionosphere conductivity within the altitude range of 50–100 km (which is a crucial range for the ELF propagation). This range is inaccessible by the most modern remote sensing equipment since it is too high for balloons and airplanes, but too low for satellites.
3) All of these models are static with time, so they do not reproduce a realistic ionosphere conductivity that constantly changes over time with the solar activity. There are some other models that change with time, such as the International Reference Ionosphere, but these provide only the background ionosphere's electron density profile and its variation [27]–[29]. Note that the ionosphere conductivity may be directly converted from the ionosphere's electron density.
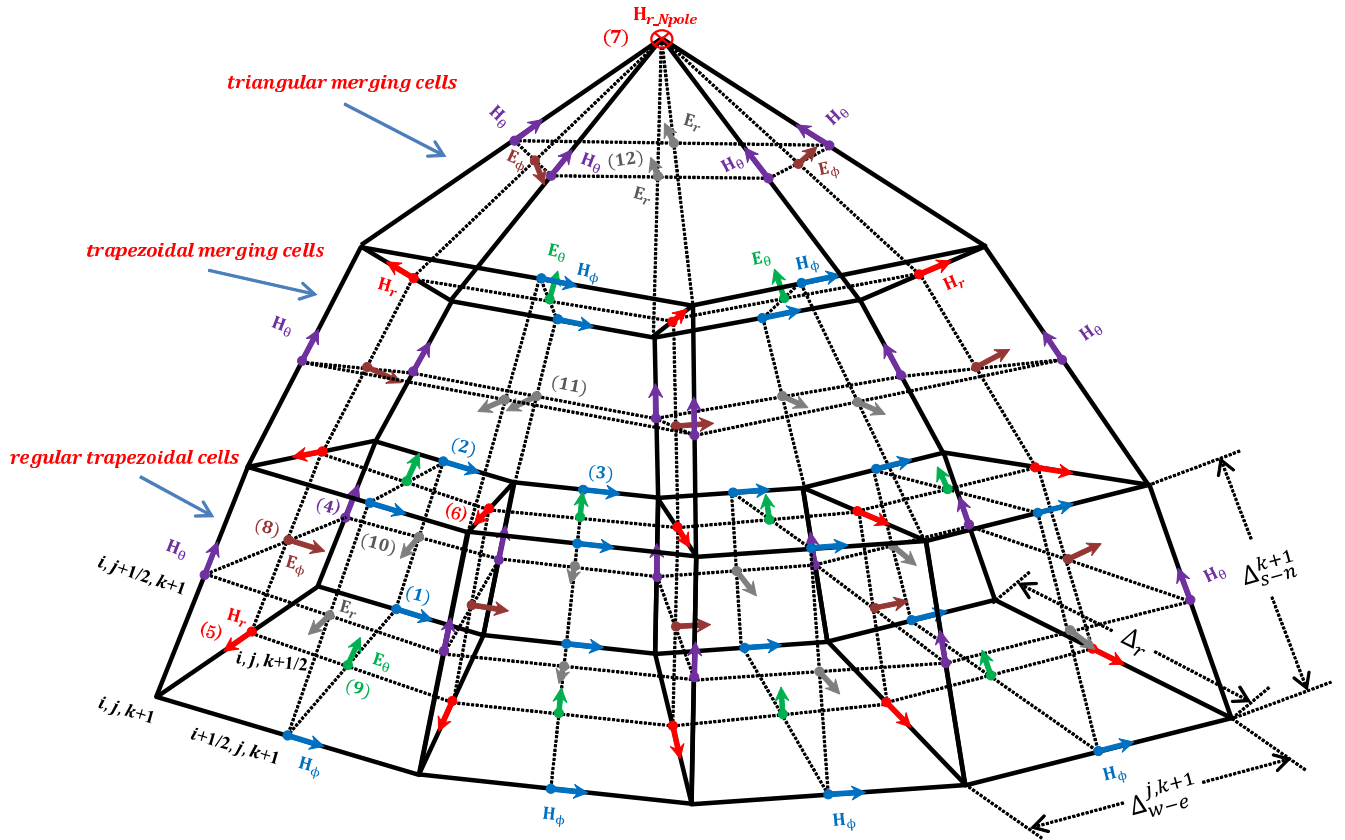
Fig. 1. FDTD grid cells in the vicinity of the North Pole. The corresponding equation number that would be used to update each field component is shown.

Instead of assuming a constant or average ionospheric state, a more comprehensive and realistic approach is to treat the ionosphere as a random medium and account for the variation of its conductivity. However, accounting for the ionosphere's conductivity uncertainties brings a significant additional computational cost. The easiest and most traditional approach is the well-known Monte Carlo (MC) method in which a large set of simulations with different samples of the random parameters is used to collect quantitative information on the statistical behavior of the model. A deterministic simulation of the wave propagation in the earth–ionosphere cavity may take hours/days for many scenarios even with the support of supercomputers, this turns out to be extremely inefficient when applying the MC method as it requires long simulation time and, thus, prevents us from its application to the analysis of complex realistic ionosphere structures. Therefore, the requirement of the computational efficiency is recognized as a critical aspect in the context of the earth–ionosphere modeling.

In this paper, the polynomial chaos expansion (PCE) technique [30] and [31] is used to efficiently account for the variability of the ionosphere conductivity in a global FDTD earth–ionosphere waveguide model. Specifically, the Galerkin-based PCE technique is used to assume a series of orthogonal polynomials of random variables for the description of the solution in a stochastic dynamical system. The PCE is a widely used method within the uncertainty quantification area and has been successfully applied to various types of problems [32]–[36]. The proposed numerical technique is

capable of treating the ionospheres complicated structure while keeping the computation cost reasonable. It is important to note that the method is particularly efficient when a small number of random input parameters are used in a large simulation, making the use of the direct method such as MC simulation infeasible.

II. MATHEMATICAL DESCRIPTION

This section first provides a brief overview of the most important aspects of the global FDTD earth–ionosphere waveguide model relevant to understanding the stochastic version. Section B describes the corresponding stochastic global FDTD algorithm that uses the Galerkin-based PCE method to take into account the variations of the ionospheric conductivity layers. Note that the formulations are derived here for only the Northern hemisphere. The algorithm for the Southern hemisphere may be derived in an analogous manner. Finally, Section C describes the methodology for calculating the global sensitivities of each input parameter on the electromagnetic fields.

A. Deterministic Model—Global FDTD Update Equations (Northern Hemisphere)

The grid is comprised of isosceles trapezoidal cells away from the North Pole and South Pole and isosceles triangular cells at the poles as shown in Fig. 1. We set M cells in the θ-direction (south to north direction), $2M$ cells in the ϕ-direction (the west to east direction) in order to

maintain square, or nearly square grid cells near the equator, and K cells in the r-direction (the radial direction that extends -100 km (below) to $+110$ km (above) sea level. The indices of the E- and H-fields extend over the following ranges:

$H_\phi(i, j, k)$ with $i \in [1, 2M]$, $j \in [1, M-1]$, $k \in [1, K+1]$

$H_\theta(i, j, k)$ with $i \in [1, 2M+1]$, $j \in [1, M]$, $k \in [1, K+1]$

$H_r(i, j, k)$ with $i \in [1, 2M+1]$ $j \in [1, M-1]$, $k \in [1, K]$

$H_{r,Npole/Spole}(k)$ with $k \in [1, K]$

$E_\phi(i, j, k)$ with $i \in [1, 2M+1]$, $j \in [1, M]$, $k \in [1, K]$

$E_\theta(i, j, k)$ with $i \in [1, 2M]$, $j \in [1, M-1]$, $k \in [1, K]$

$E_r(i, j, k)$ with $i \in [1, 2M]$, $j \in [1, M]$, $k \in [1, K+1]$.

The lattice cell dimensions along the west–east direction of each grid cell is $\Delta_{w-e}^{j,k} = \pi R_k \sin[(M-j+1)(\pi/M)]/M$, the south–north direction of each grid cell is $\Delta_{s-n}^k = \pi R_k/M$, and the radial direction of each grid cell is Δr as shown in Fig. 1, with R_k being the Earth's radius regarding to k-cell in the r-direction [16]. The space-cell eccentricity increases upon approaching either the North or South Pole, which would reduce the allowable time step since the Courant stability limit is determined by the smallest cell dimensions in the grid. To effectively mitigate this problem, pairs of adjacent cells in the west–east direction are merged several times as the grid approaches either Pole from the Equator, specifically at latitudes wherein $\Delta_{s-n}^k / \Delta_{w-e}^{j,k} \geq 2$. The illustration of merging cells is also shown in Fig. 1. Finally, a periodic boundary condition is applied to the H_θ and H_r field components along the 2-D slices of cells (over the j- and r-directions) at $i = 1$ and $i = 2M + 1$. Readers are encouraged to refer to [16] for more details.

1) H-Field Updates: Referring to Fig. 1, a regular H_ϕ-field update is

$$
\begin{aligned}
H_\phi|_{i+1/2,j,k}^{n+1/2} &= H_\phi|_{i+1/2,j,k}^{n-1/2} \\
&+ DB_{\phi 1}\big(E_\theta|_{i+1/2,j,k+1/2}^n - E_\theta|_{i+1/2,j,k-1/2}^n\big) \\
&- DB_{\phi 2}^k\big(E_r|_{i+1/2,j+1/2,k}^n - E_r|_{i+1/2,j-1/2,k}^n\big)
\end{aligned}
$$
(1)

where

$$
DB_{\phi 1} = \frac{\Delta t}{\mu_0 \Delta r} \quad \text{and} \quad DB_{\phi 2}^k = \frac{\Delta t}{\mu_0 \Delta_{s-n}^k}.
$$

For a trapezoidal merging-cell H_ϕ-field update, the left and right H_ϕ at the bottom of the merging cell require separate update equations as follows (the regular update (1) for the H_ϕ maybe applied at the top of the merging cell):

$$
\begin{aligned}
H_\phi|_{i+1/2,j+1,k}^{n+1/2} &= H_\phi|_{i+1/2,j,k}^{n-1/2} \\
&+ DB_{\phi 1}\big(E_\theta|_{i+1/2,j+1,k+1/2}^n - E_\theta|_{i+1/2,j+1,k-1/2}^n\big) \\
&- DB_{\phi 2}^k\left(\frac{3E_r|_{i+1,j+3/2,k}^n + E_r|_{i-1,j+3/2,k}^n}{4}\right. \\
&\left. - E_r|_{i+1/2,j+1/2,k}^n\right)
\end{aligned}
$$
(2)

$$
\begin{aligned}
H_\phi|_{i+3/2,j+1,k}^{n+1/2} &= H_\phi|_{i+3/2,j,k}^{n-1/2} \\
&+ DB_{\phi 1}\big(E_\theta|_{i+3/2,j+1,k+1/2}^n - E_\theta|_{i+3/2,j+1,k-1/2}^n\big) \\
&- DB_{\phi 2}^k\left(\frac{3E_r|_{i+1,j+3/2,k}^n + E_r|_{i+3,j+3/2,k}^n}{4}\right. \\
&\left. - E_r|_{i+3/2,j+1/2,k}^n\right).
\end{aligned}
$$
(3)

The H_ϕ-field update for triangular cells is analogous to (1)–(3) (depending on whether the triangular cells are merging cells or not). In the case of merging triangular cells, equations analogous to (2) and (3) are used, and in the nonmerging case, an equation analogous to (1) is used.

Next, the H_θ-field updates for regular, merging cell, and triangular cells are identical, and are as follows:

$$
\begin{aligned}
H_\theta|_{i,j+1/2,k}^{n+1/2} &= H_\theta|_{i,j+1/2,k}^{n-1/2} \\
&+ DB_{\theta 1}^{j+1/2,k}\big(E_r|_{i+1/2,j+1/2,k}^n - E_r|_{i-1/2,j+1/2,k}^n\big) \\
&- DB_{\theta 2}\big(E_\phi|_{i,j+1/2,k+1/2}^n - E_\phi|_{i,j+1/2,k-1/2}^n\big)
\end{aligned}
$$
(4)

where

$$
DB_{\theta 1}^{j+1/2,k} = \frac{\Delta t}{\mu_0 \Delta_{w-e}^{j+1/2,k}} \quad \text{and} \quad DB_{\theta 2} = \frac{\Delta t}{\mu_0 \Delta r}.
$$

The regular H_r-field update is

$$
\begin{aligned}
H_r|_{i,j,k+1/2}^{n+1/2} &= H_r|_{i,j,k+1/2}^{n-1/2} \\
&+ DB_{r1}^{k+1/2}\left(E_\phi|_{i,j+1/2,k+1/2}^n \frac{\Delta_{w-e}^{j+1/2,k+1/2}}{\Delta_{w-e}^{j,k+1/2}}\right. \\
&\left. - E_\phi|_{i,j-1/2,k+1/2}^n \frac{\Delta_{w-e}^{j-1/2,k+1/2}}{\Delta_{w-e}^{j,k+1/2}}\right) \\
&- DB_{r2}^{j,k+1/2}\big(E_\theta|_{i+1/2,j,k+1/2}^n - E_\theta|_{i-1/2,j,k+1/2}^n\big)
\end{aligned}
$$
(5)

where

$$
DB_{r1}^{k+1/2} = \frac{\Delta t}{\mu_0 \Delta_{s-n}^{k+1/2}} \quad \text{and} \quad DB_{r2}^{j,k+1/2} = \frac{\Delta t}{\mu_0 \Delta_{w-e}^{j,k+1/2}}.
$$

For triangular and trapezoidal merging cells, only the middle H_r-fields at the bottom of the merging cells require new update equation as follows:

$$
\begin{aligned}
H_r|_{i+1,j+1,k+1/2}^{n+1/2} &= H_r|_{i+1,j+1,k+1/2}^{n-1/2} + DB_{r1}^{k+1/2} \\
&\times \left(\frac{E_\phi|_{i+2,j+3/2,k+1/2}^n + E_\phi|_{i,j+3/2,k+1/2}^n}{2} \frac{\Delta_{w-e}^{j+3/2,k+1/2}}{\Delta_{w-e}^{j+1,k+1/2}}\right. \\
&\left. - E_\phi|_{i+1,j+1/2,k+1/2}^n \frac{\Delta_{w-e}^{j+1/2,k+1/2}}{\Delta_{w-e}^{j+1,k+1/2}}\right) \\
&- DB_{r2}^{j+1,k+1/2}\big(E_\theta|_{i+3/2,j+1,k+1/2}^n - E_\theta|_{i+1/2,j+1,k+1/2}^n\big).
\end{aligned}
$$
(6)

The H_r-field update at the North Pole is

$$
\begin{aligned}
H_{r,Npole}|_{1,M+1,k+1/2}^{n+1/2} &= H_{r,Npole}|_{1,M+1,k+1/2}^{n-1/2} \\
&- \frac{4\tan(\pi/N_{E\phi,Npole})\Delta t}{N_{E\phi,Npole}\Delta_{w-e}^{M+1/2,k+1/2}\mu_0} \\
&\times \sum_{X=1}^{N_{E\phi,Npole}} E_\phi|_{X,M+1/2,k+1/2}^{n} \quad (7)
\end{aligned}
$$

where $N_{E\phi,Npole}$ is the number of E_ϕ-components surrounding the $H_{r,Npole}$-component at the North Pole.

2) E-Field Updates: Similarly, referring to Fig. 1, the regular E_ϕ-field update is

$$
\begin{aligned}
E_\phi|_{i,j+1/2,k+1/2}^{n+1} &= CA_\phi^{i,j+1/2,k+1/2} E_\phi|_{i,j+1/2,k+1/2}^{n} \\
&+ CB_{\phi 1}^{i,j+1/2,k+1/2}\big(H_r|_{i,j+1,k+1/2}^{n+1/2} - H_r|_{i,j,k+1/2}^{n+1/2}\big) \\
&- CB_{\phi 2}^{i,j+1/2,k+1/2}\big(H_\theta|_{i,j+1/2,k+1}^{n+1/2} - H_\theta|_{i,j+1/2,k}^{n+1/2}\big). \quad (8)
\end{aligned}
$$

Equation (8) will be also used for trapezoidal merging cells and triangular cells E_ϕ-field updates.

Next, similar with the H_θ update, all the E_θ-field updates for regular cells, trapezoidal merging cell, or triangular cell use identical update equation given by

$$
\begin{aligned}
E_\theta|_{i+1/2,j,k+1/2}^{n+1} &= CA_\theta^{i+1/2,j,k+1/2} E_\theta|_{i+1/2,j,k+1/2}^{n} \\
&+ CB_{\theta 1}^{i+1/2,j,k+1/2}\big(H_\phi|_{i+1/2,j,k+1}^{n+1/2} - H_\phi|_{i+1/2,j,k}^{n+1/2}\big) \\
&- CB_{\theta 2}^{i+1/2,j,k+1/2}\big(H_r|_{i+1,j,k+1/2}^{n+1/2} - H_r|_{i,j,k+1/2}^{n+1/2}\big). \quad (9)
\end{aligned}
$$

Finally, the E_r-field update for regular cells is

$$
\begin{aligned}
E_r|_{i+1/2,j+1/2,k}^{n+1} &= CA_r^{i+1/2,j+1/2,k} E_r|_{i+1/2,j+1/2,k}^{n} \\
&+ CB_{r1}^{i+1/2,j+1/2,k}\big(H_\theta|_{i+1,j+1/2,k}^{n+1/2} - H_\theta|_{i,j+1/2,k}^{n+1/2}\big) \\
&- CB_{r2}^{i+1/2,j+1/2,k}\Bigg(H_\phi|_{i+1/2,j+1,k}^{n+1/2}\frac{\Delta_{w-e}^{j+1,k}}{\Delta_{w-e}^{j+1/2,k}} \\
&\qquad\qquad - H_\phi|_{i+1/2,j,k}^{n+1/2}\frac{\Delta_{w-e}^{j,k}}{\Delta_{w-e}^{j+1/2,k}}\Bigg). \quad (10)
\end{aligned}
$$

For trapezoidal merging cells is followed by

$$
\begin{aligned}
E_r|_{i+1,j+3/2,k}^{n+1} &= CA_r^{i+1,j+3/2,k} E_r|_{i+1,j+3/2,k}^{n} \\
&+ CB_{r1}^{i+1,j+3/2,k}\big(H_\theta|_{i+3,j+3/2,k}^{n+1/2} - H_\theta|_{i,j+3/2,k}^{n+1/2}\big) \\
&- CB_{r2}^{i+1,j+3/2,k}\Bigg(H_\phi|_{i+1,j+2,k}^{n+1/2}\frac{\Delta_{w-e}^{j+2,k}}{\Delta_{w-e}^{j+3/2,k}} \\
&\quad - \frac{H_\phi|_{i+1/2,j+1,k}^{n+1/2} + H_\phi|_{i+3/2,j+1,k}^{n+1/2}}{2}\frac{\Delta_{w-e}^{j+1,k}}{\Delta_{w-e}^{j+3/2,k}}\Bigg). \quad (11)
\end{aligned}
$$

And for triangular merging cells is derived by

$$
\begin{aligned}
E_r|_{i+2,M+1/2,k}^{n+1} &= CA_r^{i+2,M+1/2,k} E_r|_{i+2,M+1/2,k}^{n} \\
&+ CB_{r1}^{i+2,M+1/2,k}\big(H_\theta|_{i+4,M+1/2,k}^{n+1/2} - H_\theta|_{i,M+1/2,k}^{n+1/2}\big) \\
&+ CB_{r2}^{i+2,M+1/2,k}\frac{H_\phi|_{i+1,M,k}^{n+1/2} + H_\phi|_{i+3,M,k}^{n+1/2}}{2}. \quad (12)
\end{aligned}
$$

All the coefficients in the *E*-field update equations are given by (13), as shown at the bottom of this page, with $\alpha = \cos^{-1}[(\Delta_{w-e}^{M,k}/2\Delta_{s-n}^{k})]$. All 12 equations mentioned above form a complete set of update equations for the global FDTD earth–ionosphere waveguide model. For convenience, the corresponding equation number that would be used to update each field component is shown in Fig. 1.

B. Stochastic Model—Global PCE-FDTD Update Equations (Northern Hemisphere)

The polynomial chaos method expands the uncertain field components (E, H) as a truncated summation of orthogonal basis functions ψ_a, which are chosen from the Weiner–Askey scheme [31]. With $u = \phi, \theta, r$; we set

$$
H_u = \sum_{a=0}^{P} h_u^a \psi_a(\boldsymbol{\xi}) \quad (14)
$$

$$
E_u = \sum_{a=0}^{P} e_u^a \psi_a(\boldsymbol{\xi}) \quad (15)
$$

where h_u^a, e_u^a are the weighting coefficients. For the case of N mutually independent input variables, i.e., $\boldsymbol{\xi} = \xi_1, \xi_2, ..., \xi_N$,

$$
\begin{aligned}
CA_\phi^{i,j+1/2,k+1/2} &= \frac{1 - \frac{\tilde{\sigma}_{i,j+1/2,k+1/2}\Delta t}{2\epsilon_0}}{1 + \frac{\tilde{\sigma}_{i,j+1/2,k+1/2}\Delta t}{2\epsilon_0}}, \quad
CB_{\phi 1}^{i,j+1/2,k+1/2} = \frac{\frac{\Delta t}{\epsilon_0 \Delta_{s-n}^{k+1/2}}}{1 + \frac{\tilde{\sigma}_{i,j+1/2,k+1/2}\Delta t}{2\epsilon_0}}, \quad
CB_{\phi 2}^{i,j+1/2,k+1/2} = \frac{\frac{\Delta t}{\epsilon_0 \Delta r}}{1 + \frac{\tilde{\sigma}_{i,j+1/2,k+1/2}\Delta t}{2\epsilon_0}} \\[2ex]
CA_\theta^{i+1/2,j,k+1/2} &= \frac{1 - \frac{\tilde{\sigma}_{i+1/2,j,k+1/2}\Delta t}{2\epsilon_0}}{1 + \frac{\tilde{\sigma}_{i+1/2,j,k+1/2}\Delta t}{2\epsilon_0}}, \quad
CB_{\theta 1}^{i+1/2,j,k+1/2} = \frac{\frac{\Delta t}{\epsilon_0 \Delta r}}{1 + \frac{\tilde{\sigma}_{i+1/2,j,k+1/2}\Delta t}{2\epsilon_0}}, \quad
CB_{\theta 2}^{i+1/2,j,k+1/2} = \frac{\frac{\Delta t}{\epsilon_0 \Delta_{w-e}^{j,k+1/2}}}{1 + \frac{\tilde{\sigma}_{i+1/2,j,k+1/2}\Delta t}{2\epsilon_0}} \\[2ex]
CA_r^{i+1/2,j+1/2,k} &= \frac{1 - \frac{\tilde{\sigma}_{i+1/2,j+1/2,k}\Delta t}{2\epsilon_0}}{1 + \frac{\tilde{\sigma}_{i+1/2,j+1/2,k}\Delta t}{2\epsilon_0}}, \quad
CB_{r1}^{i+1/2,j+1/2,k} = \frac{\frac{\Delta t}{\epsilon_0 \Delta_{w-e}^{j+1/2,k}}}{1 + \frac{\tilde{\sigma}_{i+1/2,j+1/2,k}\Delta t}{2\epsilon_0}}, \quad
CB_{r2}^{i+1/2,j+1/2,k} = \frac{\frac{\Delta t}{\epsilon_0 \Delta_{s-n}^{k}}}{1 + \frac{\tilde{\sigma}_{i+1/2,j+1/2,k}\Delta t}{2\epsilon_0}} \\[2ex]
CA_r^{i+2,M+1/2,k} &= \frac{1 - \frac{\tilde{\sigma}_{i+2,M+1/2,k}\Delta t}{2\epsilon_0}}{1 + \frac{\tilde{\sigma}_{i+2,M+1/2,k}\Delta t}{2\epsilon_0}}, \quad
CB_{r1}^{i+2,M+1/2,k} = \frac{\frac{2\Delta t}{\epsilon_0 \Delta_{w-e}^{M,k}\sin\alpha}}{1 + \frac{\tilde{\sigma}_{i+2,M+1/2,k}\Delta t}{2\epsilon_0}}, \quad
CB_{r2}^{i+2,M+1/2,k} = \frac{\frac{2\Delta t}{\epsilon_0 \Delta_{s-n}^{k}\sin\alpha}}{1 + \frac{\tilde{\sigma}_{i+2,M+1/2,k}\Delta t}{2\epsilon_0}} \quad (13)
\end{aligned}
$$

TABLE I
POLYNOMIALS CHAOS BASIS FOR THE CASE OF THREE INDEPENDENT RANDOM VARIABLES ($N = 3$, $\boldsymbol{\xi} = [\xi_1, \xi_2, \xi_3]$) AND A SECOND-ORDER EXPANSION ($D = 2$)

Index b	Order D	b^{th} basis ψ_b	$\langle \psi_b^2 \rangle$
0	0	1	1
1	1	ξ_1	1
2	1	ξ_2	1/3
3	1	ξ_3	1/3
4	2	$\xi_1^2 - 1$	2
5	2	$\xi_1 \xi_2$	1/3
6	2	$\xi_1 \xi_3$	1/3
7	2	$\frac{1}{2}(3\xi_2^2 - 1)$	1/5
8	2	$\xi_2 \xi_3$	1/9
9	2	$\frac{1}{2}(3\xi_3^2 - 1)$	1/5

the multivariate polynomial chaos basis function may be expressed as

$$\psi_a(\boldsymbol{\xi}) = \prod_{i=1}^{N} \Phi_{m_i^a}(\xi_i) \tag{16}$$

where $\Phi_{m_i^a}(\xi_i)$ is a 1-D orthogonal polynomial in ξ_i and m_i^a is the multiindex corresponding to the order of the expansion for $a = 0, ..., P$. The number of terms is given by

$$P + 1 = \frac{(N + D)!}{N! D!} \tag{17}$$

where D is the highest polynomial order in the expansion.

The orthogonality property of the polynomials is expressed by

$$\langle \psi_a(\boldsymbol{\xi}), \psi_b(\boldsymbol{\xi}) \rangle = \langle \psi_b^2(\boldsymbol{\xi}) \rangle \delta_{a,b} \tag{18}$$

where $\delta_{a,b}$ is the Kronecker delta function ($\delta_{a,b} = 0$ if $a \neq b$ and $\delta_{a,b} = 1$ if $a = b$), and $\langle ., . \rangle$ denotes the ensemble average, which is the inner product in the Hilbert space and is defined as

$$\langle f(\boldsymbol{\xi}), g(\boldsymbol{\xi}) \rangle = \int f(\boldsymbol{\xi}) g(\boldsymbol{\xi}) \rho(\boldsymbol{\xi}) d(\boldsymbol{\xi}) \tag{19}$$

where $\rho(\boldsymbol{\xi})$ is the probability weighting function [31]. To evaluate the coefficients, h_u^a and e_u^a, the Galerkin method is used. This method takes inner products of expansions with the test function $\psi_b(\boldsymbol{\xi})$ (where $b = 0, ..., P$) as follows:

$$h_u^b = \frac{\langle H_u, \psi_b(\boldsymbol{\xi}) \rangle}{\langle \psi_b^2(\boldsymbol{\xi}) \rangle} \quad \text{and} \quad e_u^b = \frac{\langle E_u, \psi_b(\boldsymbol{\xi}) \rangle}{\langle \psi_b^2(\boldsymbol{\xi}) \rangle}. \tag{20}$$

Note that the choice of $\Phi_{m_i^a}(\xi_i)$ depends on the distribution of the random variable ξ_i and follows the Weiner–Askey scheme. For example, Gaussian distributed inputs are associated with Hermite polynomials and uniformly distributed inputs with Legendre polynomials. Table I summarizes the polynomial chaos basis functions truncated in the order $D = 2$, for $N = 3$ (where ξ_1 is Gaussian distributed and ξ_2, ξ_3 are uniformly distributed).

Once the coefficients e_u^a and h_u^a are found, the mean and variance of the output fields may be directly obtained. For example, the mean and variance of the E-fields may be calculated as follows. First, since $\psi_0(\boldsymbol{\xi}) = 1$ and applying the orthogonality property of the polynomials, the mean value

is derived as

$$\mu[E_u(\boldsymbol{\xi})] = \left\langle \sum_{a=0}^{P} e_u^a \psi_a(\boldsymbol{\xi}) \right\rangle = \sum_{a=0}^{P} e_u^a \langle \psi_a(\boldsymbol{\xi}) \psi_0(\boldsymbol{\xi}) \rangle$$

$$= \sum_{a=0}^{P} e_u^a \langle \psi_0^2(\boldsymbol{\xi}) \rangle \delta_{a0} = e_u^0. \tag{21}$$

Second, since the variance of a random variable x can be expressed as the mean of the square minus the square of the mean (i.e., $\sigma^2(x) = \mu(x^2) - \mu(x)^2$), we have

$$\sigma^2[E_u(\boldsymbol{\xi})] = \mu[E_u^2(\boldsymbol{\xi})] - \mu[E_u(\boldsymbol{\xi})]^2$$

$$= \sum_{a=0}^{P} (e_u^a)^2 \langle \psi_a^2(\boldsymbol{\xi}) \rangle - (e_u^0)^2 = \sum_{a=1}^{P} (e_u^a)^2 \langle \psi_a^2(\boldsymbol{\xi}) \rangle. \tag{22}$$

In summary, the first coefficient ($a = 0$) represents the mean value of the field, and the variance value of the field may be obtained from the remaining coefficients ($a = 1, \ldots, P$).

To derive the stochastic update equations for the global FDTD earth–ionosphere waveguide model, the approach described earlier is applied to all of the update equations of Section II-A. Note that none of H-field update equations of Section II-A contain the electrical conductivity parameter, which is the only uncertainty input parameter. Therefore, the stochastic update equations for all of the H-field components have an analogous form as the deterministic update equations. This is due to the orthogonality condition of (18). For example, the stochastic update equation for both regular and merging cell H_θ-fields (for both trapezoidal and triangular cells) is given as

$$h_\theta^b \big|_{i,j+1/2,k}^{n+1/2}$$

$$= h_\theta^b \big|_{i,j+1/2,k}^{n-1/2}$$

$$+ DB_{\theta 1}^{j+1/2,k} (e_r^b \big|_{i+1/2,j+1/2,k}^{n} - e_r^b \big|_{i-1/2,j+1/2,k}^{n})$$

$$- DB_{\theta 2} (e_\phi^b \big|_{i,j+1/2,k+1/2}^{n} - e_\phi^b \big|_{i,j+1/2,k-1/2}^{n}). \tag{23}$$

On the other hand, as seen in (13), all of the coefficients (CA_u, CB_{u1}, and CB_{u2}, with $u = \phi, \theta, r$) of the E-field update equations include the electrical conductivity parameter ($\tilde{\sigma}_{i,j,k}$) in which may have spatial uncertainty. For each computational cell wherein the cell's conductivity is considered as an uncertainty (such as in the ionosphere, but not in the air region immediately above the ground), its E-field update equations are derived as shown in (24)–(28) after applying the Galerkin process.

Both regular and merging cell E_ϕ-field updates (for both trapezoidal and triangular cells):

$$e_\phi^b \big|_{i,j+1/2,k+1/2}^{n+1}$$

$$= \frac{1}{\langle \psi_b^2 \rangle} \sum_{a=0}^{P} \left[e_\phi^a \big|_{i,j+1/2,k+1/2}^{n} \langle CA_\phi^{i,j+1/2,k+1/2}(\boldsymbol{\xi}) \psi_a(\boldsymbol{\xi}) \psi_b(\boldsymbol{\xi}) \rangle \right.$$

$$+ (h_r^a \big|_{i,j+1,k+1/2}^{n+1/2} - h_r^a \big|_{i,j,k+1/2}^{n+1/2})$$

$$\times \langle CB_{\phi 1}^{i,j+1/2,k+1/2}(\boldsymbol{\xi}) \psi_a(\boldsymbol{\xi}) \psi_b(\boldsymbol{\xi}) \rangle$$

$$- (h_\theta^a \big|_{i,j+1/2,k+1}^{n+1/2} - h_\theta^a \big|_{i,j+1/2,k}^{n+1/2})$$

$$\left. \times \langle CB_{\phi 2}^{i,j+1/2,k+1/2}(\boldsymbol{\xi}) \psi_a(\boldsymbol{\xi}) \psi_b(\boldsymbol{\xi}) \rangle \right]. \tag{24}$$
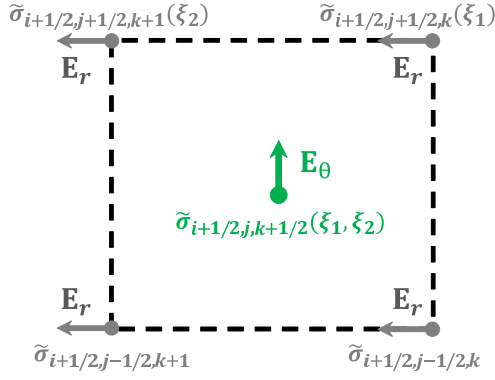
Fig. 2. E_θ-component surrounded by four mixed E_r-components with/without conductivity randomness.

Both regular and merging cell E_θ-field updates (for both trapezoidal and triangular cells):

$$e_\theta^b\big|_{i+1/2,j,k+1/2}^{n+1}$$

$$= \frac{1}{\langle \psi_b^2 \rangle} \sum_{a=0}^{P} \Bigg[e_\theta^a\big|_{i+1/2,j,k+1/2}^{n} \langle CA_\theta^{i+1/2,j,k+1/2}(\boldsymbol{\xi})\psi_a(\boldsymbol{\xi})\psi_b(\boldsymbol{\xi}) \rangle$$

$$+ \left(h_\phi^a\big|_{i+1/2,j,k+1}^{n+1/2} - h_\phi^a\big|_{i+1/2,j,k}^{n+1/2} \right)$$

$$\times \langle CB_{\theta1}^{i+1/2,j,k+1/2}(\boldsymbol{\xi})\psi_a(\boldsymbol{\xi})\psi_b(\boldsymbol{\xi}) \rangle$$

$$- \left(h_r^a\big|_{i+1,j,k+1/2}^{n+1/2} - h_r^a\big|_{i,j,k+1/2}^{n+1/2} \right)$$

$$\times \langle CB_{\theta2}^{i+1/2,j,k+1/2}(\boldsymbol{\xi})\psi_a(\boldsymbol{\xi})\psi_b(\boldsymbol{\xi}) \rangle \Bigg]. \tag{25}$$

Regular E_r-field updates:

$$e_r^b\big|_{i+1/2,j+1/2,k}^{n+1}$$

$$= \frac{1}{\langle \psi_b^2 \rangle} \sum_{a=0}^{P} \Bigg[e_r^a\big|_{i+1/2,j+1/2,k}^{n} \langle CA_r^{i+1/2,j+1/2,k}(\boldsymbol{\xi})\psi_a(\boldsymbol{\xi})\psi_b(\boldsymbol{\xi}) \rangle$$

$$+ \left(h_\theta^a\big|_{i+1,j+1/2,k}^{n+1/2} - h_\theta^a\big|_{i,j+1/2,k}^{n+1/2} \right)$$

$$\times \langle CB_{r1}^{i+1/2,j+1/2,k}(\boldsymbol{\xi})\psi_a(\boldsymbol{\xi})\psi_b(\boldsymbol{\xi}) \rangle$$

$$- \left(h_\phi^a\big|_{i+1/2,j+1,k}^{n+1/2} \frac{\Delta_{w-e}^{j+1,k}}{\Delta_{w-e}^{j+1/2,k}} - h_\phi^a\big|_{i+1/2,j,k}^{n+1/2} \frac{\Delta_{w-e}^{j,k}}{\Delta_{w-e}^{j+1/2,k}} \right)$$

$$\langle CB_{r2}^{i+1/2,j+1/2,k}(\boldsymbol{\xi})\psi_a(\boldsymbol{\xi})\psi_b(\boldsymbol{\xi}) \rangle \Bigg]. \tag{26}$$

Trapezoidal merging cell E_r-field updates:

$$e_r^b\big|_{i+1,j+3/2,k}^{n+1}$$

$$= \frac{1}{\langle \psi_b^2 \rangle} \sum_{a=0}^{P} \Bigg[e_r^a\big|_{i+1,j+3/2,k}^{n} \langle CA_r^{i+1,j+3/2,k}(\boldsymbol{\xi})\psi_a(\boldsymbol{\xi})\psi_b(\boldsymbol{\xi}) \rangle$$

$$+ \left(h_\theta^a\big|_{i+3,j+3/2,k}^{n+1/2} - h_\theta^a\big|_{i,j+3/2,k}^{n+1/2} \right)$$

$$\times \langle CB_{r1}^{i+1,j+3/2,k}(\boldsymbol{\xi})\psi_a(\boldsymbol{\xi})\psi_b(\boldsymbol{\xi}) \rangle$$

$$- \Bigg(h_\phi^a\big|_{i+1,j+2,k}^{n+1/2} \frac{\Delta_{w-e}^{j+2,k}}{\Delta_{w-e}^{j+3/2,k}}$$

$$- \frac{h_\phi^a\big|_{i+1/2,j+1,k}^{n+1/2} + h_\phi^a\big|_{i+3/2,j+1,k}^{n+1/2}}{2} \frac{\Delta_{w-e}^{j+1,k}}{\Delta_{w-e}^{j+3/2,k}} \Bigg)$$

$$\times \langle CB_{r2}^{i+1,j+3/2,k}(\boldsymbol{\xi})\psi_a(\boldsymbol{\xi})\psi_b(\boldsymbol{\xi}) \rangle \Bigg]. \tag{27}$$

Triangular cell E_r-field updates (merging cell case): Equation (28) are shown at the bottom of the previous page. All of the inner products of the three random functions may be precomputed via numerical integration before time-stepping begins. This step obviously requires some extra memory and simulation time, but its cost is negligible compared to a single run of the deterministic simulation.

To minimize the amount of memory needed, the electrical conductivities at the locations of the E_ϕ- and E_θ-components are interpolated from the conductivities at the locations of the four nearest-neighbor E_r-components (which are stored in memory). For example, consider the electrical conductivity at the location of $E_\theta^{i+1/2,j,k+1/2}$ near a material interface, specifically for a case wherein the $E_\theta^{i+1/2,j,k+1/2}$ is surrounded by a material with no conductivity randomness at two of the nearest-neighbor E_r-components, and a material with conductivities following an independent random variable ξ_1 and ξ_2 at the other two nearest-neighbor E_r-components as shown in Fig. 2. In this case, the inner product integral may be calculated according to (29). For other $E_\theta^{i+1/2,j,k+1/2}$ locations not inside or neighboring any uncertainty materials, these inner products reduce to two random functions and may then utilize the orthogonal property of the polynomial basis functions. Thus, the E-field update equations may be decoupled and

$$e_r^b\big|_{i+2,M+1/2,k}^{n+1} = \frac{1}{\langle \psi_b^2 \rangle} \sum_{a=0}^{P} \Bigg[e_r^a\big|_{i+2,M+1/2,k}^{n} \langle CA_r^{i+2,M+1/2,k}(\boldsymbol{\xi})\psi_a(\boldsymbol{\xi})\psi_b(\boldsymbol{\xi}) \rangle$$

$$+ \left(h_\theta^a\big|_{i+4,M+1/2,k}^{n+1/2} - h_\theta^a\big|_{i,M+1/2,k}^{n+1/2} \right)\langle CB_{r1}^{i+2,M+1/2,k}(\boldsymbol{\xi})\psi_a(\boldsymbol{\xi})\psi_b(\boldsymbol{\xi}) \rangle$$

$$+ \frac{h_\phi^a\big|_{i+1,M,k}^{n+1/2} + h_\phi^a\big|_{i+3,M,k}^{n+1/2}}{2}\langle CB_{r2}^{i+2,M+1/2,k}(\boldsymbol{\xi})\psi_a(\boldsymbol{\xi})\psi_b(\boldsymbol{\xi}) \rangle \Bigg] \tag{28}$$

$$\langle CB_{\theta1}^{i+1/2,j,k+1/2}(\xi_1,\xi_2)\psi_a(\xi_1,\xi_2)\psi_b(\xi_1,\xi_2) \rangle$$

$$= \int_\Gamma \frac{2\Delta t}{\Delta r[2\epsilon_0 + (\tilde{\sigma}_{i+1/2,j+1/2,k}(\xi_1) + \tilde{\sigma}_{i+1/2,j+1/2,k+1}(\xi_2) + \tilde{\sigma}_{i+1/2,j-1/2,k} + \tilde{\sigma}_{i+1/2,j-1/2,k+1})\Delta t/4]}$$

$$\times \psi_a(\xi_1,\xi_2)\psi_b(\xi_1,\xi_2)\rho(\xi_1,\xi_2)d(\xi_1)d(\xi_2) \tag{29}$$
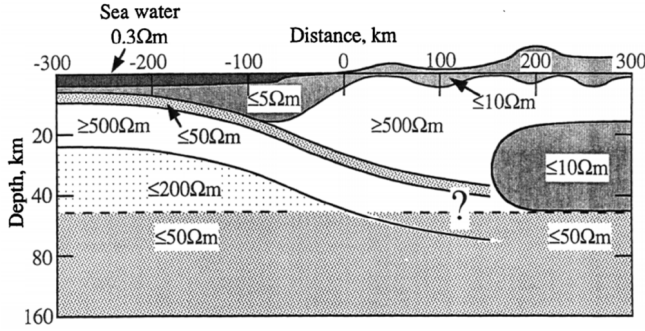
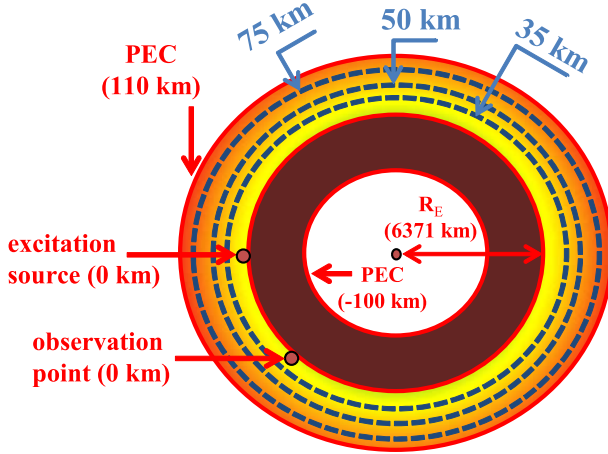Fig. 3. Conductivity values used for the lithosphere [39].

Fig. 4.   Diagram depicting the general geometry of the global FDTD model (note: not drawn to scale).

TABLE II

INPUT PARAMETERS AND UNCERTAINTY

Ionospheric cond. layer	Mean value μ	Distribution
at 35 km	$1.62 \times 10^{-11} (S/m)$	Gaussian, $\sigma = 20\%$
at 50 km	$1.16 \times 10^{-9} (S/m)$	Uniform, $\sigma = 30\%$
at 75 km	$1.44 \times 10^{-6} (S/m)$	Uniform, $\sigma = 60\%$

solved for $b = 0, ..., P$ independently, as for the H-field update equations.

C. Sensitivities

In order to analyze the impact of the uncertain inputs on the variability of the output electromagnetic field components, the Sobol decomposition is applied to (14) and (15) [37], [38]. The Sobol decomposition yields a set of conditional variances (the Sobol indices) indicating the relative contribution each combination of input parameters makes toward the uncertainty of the output E- and H-fields. Using E_r as an example, the Sobol indices for the set of inputs v, with $v \subseteq \{1, 2, ..., N\}$, are given by [38]

$$S_v = \frac{\sum_{m \in K_v} \left(e^m_{r,i+1/2,j+1/2,k}\right)^2 \langle \psi^2_m \rangle}{\sum_{a=1}^{P} \left(e^a_{r,i+1/2,j+1/2,k}\right)^2 \langle \psi^2_a \rangle} \quad (30)$$

where K_v is an index to the terms in (15) that contain v.

III. NUMERICAL EXAMPLES

To validate the new 3-D PCE-FDTD model in this paper, we first reproduce the ELF propagation characteristics reported

---

Algorithm 1 Regular FDTD Simulation

1: Calculate all coefficients using the mean values of the conductivities
2: //Begin time stepping loop
3: **for** $n = 1 \rightarrow nmax$ **do**
4:     //Calculate space loops for H-field and E-field using equations (1)-(12) as follows:
5:     **for** $i, j, k = 1, 1, 1 \rightarrow 2M,M\text{-}1,K\text{+}1$ **do**
6:         **if** $\Delta^k_{s-n}/\Delta^{j,k}_{w-e} < 2$ **then**
7:             Calculate H_ϕ-field using (1)
8:         **else**
9:             Calculate H_ϕ-field using (2), (3)
10:        **end if**
11:    **end for**
12:    **for** $i, j, k = 1, 1, 1 \rightarrow 2M\text{+}1,M,K\text{+}1$ **do**
13:        Calculate H_θ-field using (4)
14:    **end for**
15:    **for** $i, j, k = 1, 1, 1 \rightarrow 2M\text{+}1,M\text{-}1,K$ **do**
16:        **if** $\Delta^k_{s-n}/\Delta^{j,k}_{w-e} < 2$ **then**
17:            Calculate H_r-field using (5)
18:        **else**
19:            Calculate H_r-field using (6)
20:        **end if**
21:    **end for**
22:    **for** $k = 1 \rightarrow K$ **do**
23:        Calculate $H_{r,poles}$-field using (7)
24:    **end for**
25:    **for** $i, j, k = 1, 1, 1 \rightarrow 2M\text{+}1,M,K$ **do**
26:        Calculate E_ϕ-field using (8)
27:    **end for**
28:    **for** $i, j, k = 1, 1, 1 \rightarrow 2M,M\text{-}1,K$ **do**
29:        Calculate E_θ-field using (9)
30:    **end for**
31:    **for** $i, j, k = 1, 1, 1 \rightarrow 2M,M,K\text{+}1$ **do**
32:        **if** $\Delta^k_{s-n}/\Delta^{j,k}_{w-e} < 2$ **then**
33:            Calculate E_r-field using (10)
34:        **else**
35:            **if** $1 < j < M$ **then**
36:                Calculate E_r-field using (11)
37:            **else**
38:                Calculate E_r-field using (12)
39:            **end if**
40:        **end if**
41:    **end for**
42: **end for**

---

in [16]. A resolution of $40 \times 40 \times 5$ km at the equator is chosen for two reasons: 1) to keep the spatial increment (grid cell size) sufficiently small (at least 10 cells per wavelength at ELF) in order to ensure that the numerical dispersion error is negligible and 2) to resolve major topographical details. For the lithosphere, conductivity values are assigned according to Fig. 3 [39], depending on whether a grid cell coordinate is below an ocean or a continent. For the ionosphere, the exponential conductivity profile of [23] is used as shown in (31), with an additional assumption that the conductivity values have

---

Algorithm 2 MC Simulation

1: //*num_uncert*: number of conductivity uncertainties
2: **for** $nn = 1 \rightarrow num\_uncert$ **do**
3:    //*num_MC*: MC iterations
4:    **for** $m = 1 \rightarrow num\_MC$ **do**
5:       Generate and assign random values for each conductivity value $array\_cond(m, nn)$
6:    **end for**
7: **end for**
8: //Begin MC simulation
9: **for** $m = 1 \rightarrow num\_MC$ **do**
10:    Calculate all coefficients using conductivities $array\_cond(m, nn)$ determined earlier
11:    //Begin time stepping loop
12:    **for** $n = 1 \rightarrow nmax$ **do**
13:       Calculate space loops for H-field and E-field using equations (1)-(12) as shown in Algorithm 1
14:    **end for**
15: **end for**
16: **for** $n = 1 \rightarrow nmax$ **do**
17:    //Calculate mean and standard deviation values of H-field and E-field
18:    $\mu(n) = \frac{1}{num\_MC} \sum_{m=1}^{num\_MC} array(m, n)$
19:
20:    $\sigma(n) = \sqrt{\frac{1}{num\_MC} \sum_{m=1}^{num\_MC} [array(m, n) - \mu(n)]^2}$
21: **end for**

Algorithm 3 PCE Simulation

1: **for** $b = 0 \rightarrow P$ **do**
2:    Calculate $\langle \psi_b^2 \rangle$
3: **end for**
4: **for** $nn = 1 \rightarrow num\_uncert$ **do**
5:    **for** $a = 0 \rightarrow P$ **do**
6:       **for** $b = 0 \rightarrow P$ **do**
7:          Precalculate all inner products
8:       **end for**
9:    **end for**
10: **end for**
11: //Begin time stepping loop
12: **for** $n = 1 \rightarrow nmax$ **do**
13:    **for** $b = 0 \rightarrow P$ **do**
14:       Calculate space loop for H-field using (23)
15:       REGULAR_MESH = TRUE
16:       **for** $nn = 1 \rightarrow num\_uncert$ **do**
17:          **if** $i, j, k \in [i, j, k\_uncert\_start(nn) \rightarrow i, j, k\_uncert\_end(nn)]$ **then**
18:             REGULAR_MESH = FALSE
19:             Calculate E-field using (24)-(28)
20:          **end if**
21:       **end for**
22:       **if** REGULAR_MESH = TRUE **then**
23:          Calculate E-field using regular updates
24:       **end if**
25:    **end for**
26:    Calculate mean and standard deviation values of H-field and E-field and sensitivity using (21), (22) and (30)
27: **end for**

---

an uncertainty layer at the heights of 35, 50, and 75 km as shown in Fig. 4

$$\tilde{\sigma}_{\text{ionosphere}}(r) = \epsilon_0 \times 2.5 \times 10^5 \exp[-\beta(H_{\text{ref}} - r)]. \quad (31)$$

For daytime propagation condition considered in this numerical example, the inverse scale height $\beta \approx 0.285$ km^{-1} and the reference height $H_{\text{ref}} \approx 74$ km. The uncertainty parameters behave as three independent random variables with distributions and statistical values as given in Table II.

The excitation source is a vertical, 5-km-long current pulse having a Gaussian time-waveform with a $1/e$ full width of $480\Delta t$, where $\Delta t = 3.0\mu$s. It is located just above the Earth's surface on the equator at longitude 47^0W. Algorithm 1 presents the pseudocode for a regular FDTD simulation that ignores the uncertainty of the ionosphere conductivity. First, a brute-force 1000 iterations MC simulation is run following by Algorithm 2 to make a benchmark for our model's validation. Second, PCE simulations of first- and second-order Algorithm 3 are computed. In this algorithm, a logical variable (REGULAR_MESH) is used to determine whether the grid cell contains an uncertain conductivity or not. If there is uncertainty, then the stochastic update equations (24)–(28) should be used to update the E-field components. If there is no uncertainty, then the deterministic update equations should be used for the E-field components. All the FDTD simulation parameters are summarized in Table III.

Figs. 5 and 6 illustrate time waveforms comparing the mean and standard deviation, respectively, of the radial E-field computed via the new PCE method versus the MC method.

TABLE III
FDTD SIMULATION PARAMETERS

Spatial increment	$\Delta\phi = \Delta\theta = 40$ km and $\Delta r = 5$ km
Domain size	$\phi \times \theta \times r = 1024 \times 512 \times 42$ (cells)
CFL condition number	$\Delta t_{\text{CFL}} = \frac{1}{c_0 \sqrt{\frac{1}{(\Delta\phi)^2} + \frac{1}{(\Delta\theta)^2} + \frac{1}{(\Delta r)^2}}} \approx 16.4\mu s$
Temporal increment	$\Delta t = 3.0\mu s$
Number of time steps	$nmax = 30000$
Excitation source	Gaussian time-waveform
Frequency of interest	50-500 Hz
Wavelength of interest	600-6000 km

The observation point is located on the Earth's surface at the equator directly east of the source at on-fourth of the distance to the antipode. Figs. 5 and 6 indicate that the PCE method with order $d = 1$ is already quite accurate and that the PCE results of order $d = 2$ are nearly a perfect match with the MC results.

Fig. 7 includes 20 lines of the standard deviation values based on limited sets of MC simulations (each 50 out of 1000 runs). The large variation of the lines in Fig. 7 demonstrates the need to run thousands of MC simulations in order to obtain accurate standard deviation results. A large number of MC simulations are needed because of the large variability of the input conductivity parameters shown in Table II. Even when the standard deviation of the conductivity layer at 50 and 75 km is increased to 50% and 100%, respectively, it is also quite clear that a PCE with $d = 2$ is good enough to
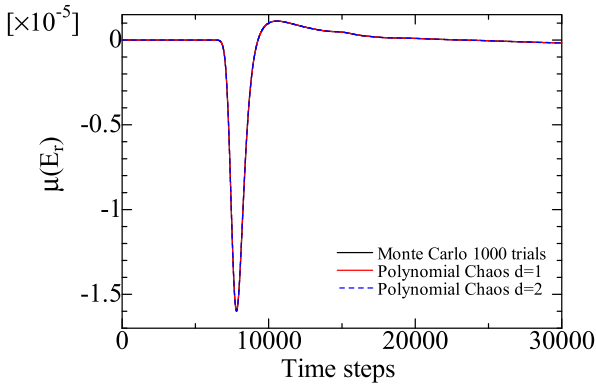
Fig. 5. Mean value of E_r (observed at the Equator located one-fourth of the distance to the antipode).
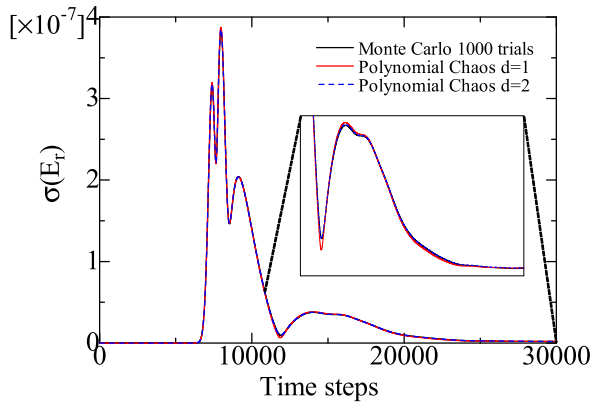

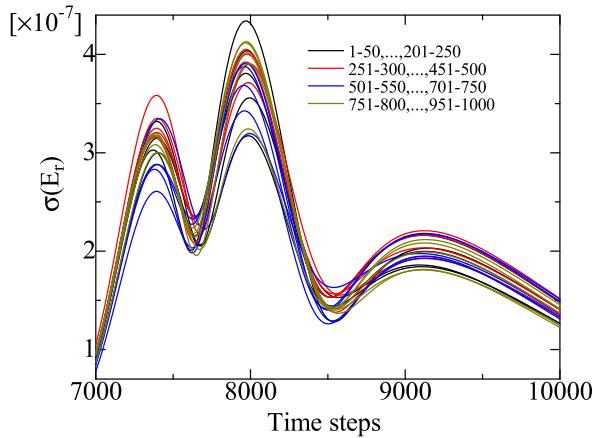Fig. 6. Standard deviation of E_r (observed at the Equator located one-fourth of the distance to the antipode).

Fig. 7. Standard deviation results obtained from each set of 50 simulations (out of the total 1000 simulations) of the MC method.
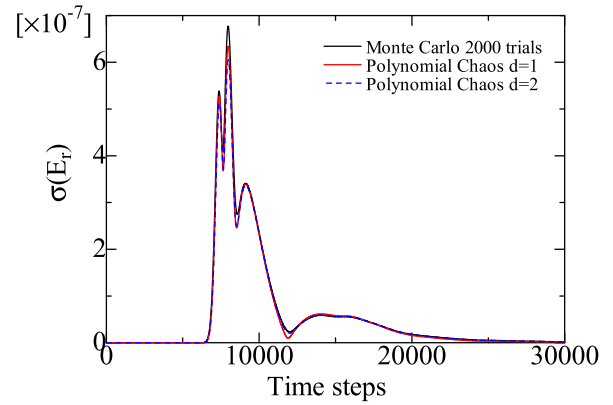

Fig. 8. Standard deviation of E_r when the standard deviation of the conductivity layer at 50 and 75 km are increased to 50% and 100%, respectively.
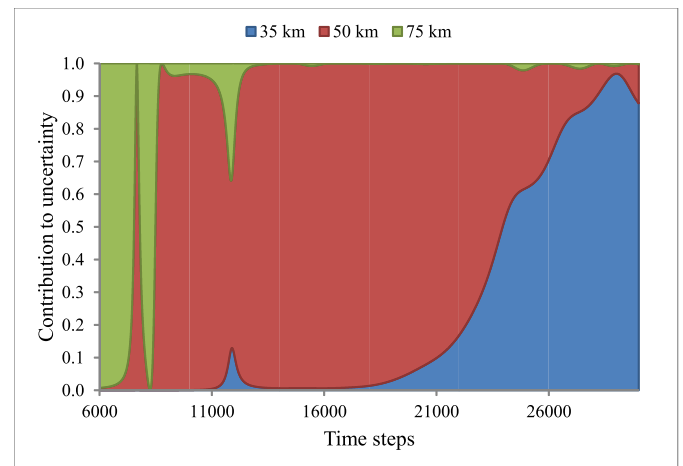

Fig. 9. Relative contribution of each ionosphere conductivity layer to the uncertainty computed using the order $d = 2$ expansion (three layers case).

capture the statistical information of the system response as shown in Fig. 8. On the other hand, the MC method required an additional one thousand simulations.

Using the approach of Section II-C, Fig. 9 shows the relative contribution that each ionosphere conductivity layer makes toward the uncertainty in E_r computed via (30). The results in this figure indicate that the variation of the output E_r-field relies mostly on the variation of the conductivity layers at 50 and 75 km during the period of $7000 - 10\,000$

time steps, where the amplitude of the ELF propagation pulse is largest. This sensitivity analysis is valuable as it indicates which layers have the greater impact on the variability of the response and play an important role in the ELF propagation. For example, Fig. 10 plots the sensitivity analysis for a test case wherein four conductivity layers at 40, 60, 80, and 100 km have an identical variability of $\sigma = 20\%$. The conductivity variations at 60 and 80 km are seen to have a larger impact than the variations at 40 and 100 km on $7000 - 10\,000$ time steps of interest. It may lead to two conclusions: first, as the atmosphere conductivity follows exponential profile, the values at 40 km are too small to affect the ELF propagation, and second, the ELF waves are reflected below 100 km (which is why the upper boundary of the grid may be set to a PEC).

Finally, Table IV compares the efficiency of the MC method to the proposed PCE-based method. Both methods are parallelized using the message passing interface standard and executed on 8 nodes with 256 cores ($8 \times 8 \times 4$ spherical division) of the Blue Waters supercomputer at the University of Illinois at Urbana–Champaign. Each compute node is composed of two AMD 6276 processors (clock speed at 2.3 GHz) and 64 GB of memory. The comparison confirms the efficiency and time savings of the PCE method over the brute-force MC approach.
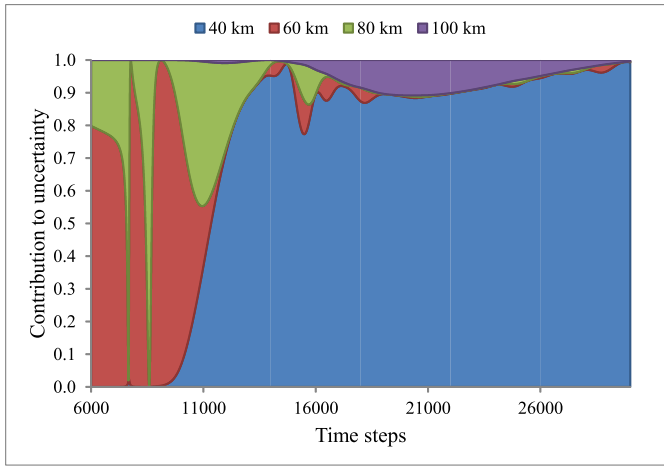
Fig. 10. Relative contribution of each ionosphere conductivity layer to the uncertainty computed using the order $d = 2$ expansion (four layers case).

TABLE IV
SIMULATION TIME REQUIRED BY THE MC AND
THE PROPOSED PCE-BASED METHODS

Method	MC 1000 runs	PCE order=1	PCE order=2
Simulation time	10 days	1 hour 49 mins	8 hours 33 mins

IV. CONCLUSION

The modeling ELF electromagnetic wave propagation in the global earth–ionosphere waveguide using the FDTD method must be as efficient as possible due to the required large number of grid cells and long simulation times (large number of time steps due to the small time step increments). In order to account for the uncertainty and variability of the ionospheric conductivity resulting from space weather events, time of day, etc., a large number of simulations are needed when utilizing the MC method. In this paper, an efficient numerical approach has been presented to calculate both the mean and variance of the electric and magnetic fields in the earth–ionosphere waveguide using the nonsampling PCE-based FDTD method. An excellent agreement was obtained between the results of the proposed method and the standard MC method. Furthermore, the proposed method was shown to be more computationally efficient than the MC approach. We believe this PCE-FDTD method can be used as a powerful numerical tool for any complex ELF propagation models since the method is applicable to any type of medium's structures, including one that is too complex to study by analytical methods.

It is worth noting that the proposed global stochastic model may be applied to localized high-resolution regions, uncertainty in the ground conductivity, or even to other planets in a straightforward manner. For example, studying Schumann resonances on planets such as Venus, Mars, Jupiter, Saturn, Titan, etc. still remains an active research area (e.g., [18], [40]–[45]). Some planets are known to have rather low ground conductivity that has a significant influence on the ELF wave propagation. In such cases, uncertainty in the ground conductivity may be included in the model due to the lack of full knowledge of the ground conductivity parameter.

The equations set we have developed here is also fully capable of studying these cases.

REFERENCES

[1] S. A. Cummer, U. S. Inan, T. F. Bell, and C. P. Barrington-Leigh, "ELF radiation produced by electrical currents in sprites," *Geophys. Res. Lett.*, vol. 25, no. 8, pp. 1281–1284, 1998.

[2] S. A. Cummer and W. M. Farrell, "Radio atmospheric propagation on Mars and potential remote sensing applications," *J. Geophys. Res., Planets*, vol. 104, no. E6, pp. 14149–14157, 1999.

[3] E. R. Williams, "The Schumann resonance: A global tropical thermometer," *Science*, vol. 256, no. 5060, pp. 1184–1187, 1992.

[4] M. Parrot, "Statistical study of ELF/VLF emissions recorded by a low-altitude satellite during seismic events," *J. Geophys. Res., Space Phys.*, vol. 99, no. A12, pp. 23339–23347, 1994.

[5] W. Harth, "Theory of low frequency wave propagation," in *CRC Handbook of Atmospherics*, vol. 2. Boca Raton, FL, USA: CRC Press, 1982, pp. 133–202.

[6] J. R. Wait, *Electromagnetic Wave Theory*. New York, NY, USA: Harper & Row, 1985.

[7] J. R. Wait, *Electromagnetic Waves in Stratified Media: Revised Edition Including Supplemented Material*, vol. 3. Amsterdam, The Netherlands: Elsevier, 2013.

[8] A. Kulak and J. Mlynarczyk, "ELF propagation parameters for the ground-ionosphere waveguide with finite ground conductivity," *IEEE Trans. Antennas Propag.*, vol. 61, no. 4, pp. 2269–2275, Apr. 2013.

[9] A. Kulak, J. Mlynarczyk, and J. Kozakiewicz, "An analytical model of ELF radiowave propagation in ground-ionosphere waveguides with a multilayered ground," *IEEE Trans. Antennas Propag.*, vol. 61, no. 9, pp. 4803–4809, Sep. 2013.

[10] A. Taflove and S. C. Hagness, *Computational Electromagnetics: Finite-Difference Time-Domain Method*, 3rd ed. Norwood, MA, USA: Artech House, 2005.

[11] M. Thèvenot, J.-P. Bérenger, T. Monedière, and F. Jecko, "A FDTD scheme for the computation of VLF-LF propagation in the anisotropic earth-ionosphere waveguide," *Annales Télécommunications*, vol. 54, nos. 5–6, pp. 297–310, 1999.

[12] J.-P. Bérenger, "FDTD computation of VLF-LF propagation in the Earth-ionosphere waveguide," *Annales Télécommunications*, vol. 57, nos. 11–12, pp. 1059–1090, 2002.

[13] S. A. Cummer, "Modeling electromagnetic propagation in the Earth-ionosphere waveguide," *IEEE Trans. Antennas Propag.*, vol. 48, no. 9, pp. 1420–1429, Sep. 2000.

[14] T. Otsuyama, D. Sakuma, and M. Hayakawa, "FDTD analysis of ELF wave propagation and Schumann resonances for a subionospheric waveguide model," *Radio Sci.*, vol. 38, no. 6, pp. 11-1–11-7, Dec. 2003.

[15] J. J. Simpson and A. Taflove, "Two-dimensional FDTD model of antipodal ELF propagation and Schumann resonance of the Earth," *IEEE Antennas Wireless Propag. Lett.*, vol. 1, no. 1, pp. 53–56, 2002.

[16] J. J. Simpson and A. Taflove, "Three-dimensional FDTD modeling of impulsive ELF propagation about the earth-sphere," *IEEE Trans. Antennas Propag.*, vol. 52, no. 2, pp. 443–451, Feb. 2004.

[17] H. Yang and V. P. Pasko, "Three-dimensional finite difference time domain modeling of the Earth-ionosphere cavity resonances," *Geophys. Res. Lett.*, vol. 32, no. 3, p. L03114, Feb. 2005.

[18] H. Yang, V. P. Pasko, and Y. Yair, "Three-dimensional finite difference time domain modeling of the Schumann resonance parameters on Titan, Venus, and Mars," *Radio Sci.*, vol. 41, no. 2, pp. 1–10, Apr. 2006.

[19] B. T. Nguyen, C. Furse, and J. J. Simpson, "Analysis of electromagnetic field variability in magnetized ionosphere plasma using the stochastic FDTD method," in *Proc. IEEE Antennas Propag. Soc. Int. Symp.*, Memphis, TN, USA, Jul. 2014, pp. 3–4.

[20] B. T. Nguyen, C. Furse, and J. J. Simpson, "A 3-D stochastic FDTD model of electromagnetic wave propagation in magnetized ionosphere plasma," *IEEE Trans. Antennas Propag.*, vol. 63, no. 1, pp. 304–313, Jan. 2015.

[21] B. T. Nguyen, A. Samimi, S. W. Vergara, C. D. Sarris, and J. J. Simpson, "Analysis of electromagnetic wave propagation in variable magnetized plasma via polynomial chaos expansion," *IEEE Trans. Antennas Propag.*, to be published.

[22] R. K. Cole, Jr., and E. T. Pierce, "Electrification in the Earth's atmosphere for altitudes between 0 and 100 kilometers," *J. Geophys. Res.*, vol. 70, no. 12, pp. 2735–2749, 1965.

[23] P. R. Bannister, "The determination of representative ionospheric conductivity parameters for ELF propagation in the Earth-ionosphere waveguide," *Radio Sci.*, vol. 20, no. 4, pp. 977–984, 1985.

[24] P. R. Bannister, "Further examples of seasonal variations of ELF radio propagation parameters," *Radio Sci.*, vol. 34, no. 1, pp. 199–208, 1999.

[25] V. C. Mushtak and E. R. Williams, "ELF propagation parameters for uniform models of the Earth–ionosphere waveguide," *J. Atmos. Solar-Terr. Phys.*, vol. 64, no. 18, pp. 1989–2001, 2002.

[26] A. P. Nickolaenko, Y. P. Galuk, and M. Hayakawa, "Vertical profile of atmospheric conductivity that matches Schumann resonance observations," *SpringerPlus*, vol. 5, no. 1, p. 108, 2016.

[27] D. Bilitza and B. W. Reinisch, "International reference ionosphere 2007: Improvements and new parameters," *Adv. Space Res.*, vol. 42, no. 4, pp. 599–609, 2008.

[28] D. Bilitza, L.-A. McKinnell, B. Reinisch, and T. Fuller-Rowell, "The international reference ionosphere today and in the future," *J. Geodesy*, vol. 85, no. 12, pp. 909–920, 2011.

[29] D. Bilitza *et al.*, "The international reference ionosphere 2012—A model of international collaboration," *J. Space Weather Space Clim.*, vol. 4, Feb. 2014, Art. no. A07.

[30] R. G. Ghanem and P. Spanos, *Stochastic Finite Elements: A Spectral Approach*. New York, NY, USA: Springer-Verlag, 1991.

[31] D. Xiu and G. E. Karniadakis, "The Wiener–Askey polynomial chaos for stochastic differential equations," *SIAM J. Sci. Comput.*, vol. 24, no. 2, pp. 619–644, 2002.

[32] R. S. Edwards, A. C. Marvin, and S. J. Porter, "Uncertainty analyses in the finite-difference time-domain method," *IEEE Trans. Electromagn. Compat.*, vol. 52, no. 1, pp. 155–163, Feb. 2010.

[33] A. C. M. Austin, N. Sood, J. Siu, and C. D. Sarris, "Application of polynomial chaos to quantify uncertainty in deterministic channel models," *IEEE Trans. Antennas Propag.*, vol. 61, no. 11, pp. 5754–5761, Nov. 2013.

[34] A. C. M. Austin and C. D. Sarris, "Efficient analysis of geometrical uncertainty in the FDTD method using polynomial chaos with application to microwave circuits," *IEEE Trans. Microw. Theory Techn.*, vol. 61, no. 12, pp. 4293–4301, Dec. 2013.

[35] Z. Zhang, T. A. El-Moselhy, I. M. Elfadel, and L. Daniel, "Stochastic testing method for transistor-level uncertainty quantification based on generalized polynomial chaos," *IEEE Trans. Comput.-Aided Design Integr. Circuits Syst.*, vol. 32, no. 10, pp. 1533–1545, Oct. 2013.

[36] B. T. Nguyen, A. Samimi, and J. J. Simpson, "A polynomial chaos approach for EM uncertainty propagation in 3D-FDTD magnetized cold plasma," in *Proc. IEEE Symp. Electromagn. Compat. Signal Integr.*, Santa Clara, CA, USA, Mar. 2015, pp. 1–5.

[37] B. Sudret, "Global sensitivity analysis using polynomial chaos expansions," *Rel. Eng. Syst. Safety*, vol. 93, no. 7, pp. 964–979, Jul. 2008.

[38] T. Crestaux, O. Le Maître, and J.-M. Martinez, "Polynomial chaos expansion for sensitivity analysis," *Rel. Eng. Syst. Saf.*, vol. 94, no. 7, pp. 1161–1172, 2009.

[39] J. F. Hermance, "Electrical conductivity models of the crust and mantle," in *Global Earth Physics: A Handbook of Physical Constants*. Hoboken, NJ, USA: Wiley, 1995, pp. 190–205.

[40] O. Pechony and C. Price, "Schumann resonance parameters calculated with a partially uniform knee model on Earth, Venus, Mars, and Titan," *Radio Sci.*, vol. 39, no. 5, p. RS5007, 2004.

[41] G. J. Molina-Cuberos *et al.*, "Schumann resonances as a tool to study the lower ionospheric structure of Mars," *Radio Sci.*, vol. 41, no. 1, p. RS1003, Feb. 2006.

[42] F. Simões *et al.*, "The Schumann resonance: A tool for exploring the atmospheric environment and the subsurface of the planets and their satellites," *Icarus*, vol. 194, no. 1, pp. 30–41, 2008.

[43] C. Béghin *et al.*, "New insights on Titan's plasma-driven Schumann resonance inferred from Huygens and Cassini data," *Planet. Space Sci.*, vol. 57, nos. 14–15, pp. 1872–1888, 2009.

[44] C. Béghin *et al.*, "Analytic theory of Titan's Schumann resonance: Constraints on ionospheric conductivity and buried water ocean," *Icarus*, vol. 218, no. 2, pp. 1028–1042, 2012.

[45] J. Kozakiewicz, A. Kulak, and J. Mlynarczyk, "Analytical modeling of Schumann resonance and ELF propagation parameters on Mars with a multi-layered ground," *Planet. Space Sci.*, vol. 117, pp. 127–135, Nov. 2015.

Bach T. Nguyen received the B.Eng. and M.Eng. degrees in electrical engineering from the National Defense Academy of Japan, Yokosuka, Japan, in 2007 and 2009, respectively, and the Ph.D. degree in electrical engineering from the University of Utah, Salt Lake City, UT, USA, in 2017.

His current research interests include computational electromagnetics, uncertainty quantification, RF/Microwave technology, plasma physics, and liquid crystal.

Dr. Nguyen was a recipient of the IEEE Antennas and Propagation Society (AP-S) Doctoral Research Award and Honorable Mention in the Student Paper Competition of the 2014 IEEE AP-S International Symposium in Memphis, TN, USA.

Stephen E. Wiechecki Vergara (M'09) received the B.S. and M.S. degrees in mathematics from the University of Texas at San Antonio, San Antonio, TX, USA, in 1991 and 1993, respectively, the Ph.D. degree in statistical science from Southern Methodist University, Dallas, TX, USA, in 1998, and the M.S. degree in electrical engineering from the University of Central Florida, Orlando, FL, USA, in 2005.

He is currently the Director of Scientific Research/Analysis with Perspecta, Melbourne, FL, Australia, where he oversees a team of scientists with diverse backgrounds in digital signal and image processing, statistics, machine learning, radar, electrooptics, computational electromagnetics, high-performance computing, and astrophysics.

Costas D. Sarris (SM'08) received the Ph.D. degree in electrical engineering and the M.Sc. degree in applied mathematics from the University of Michigan, Ann Arbor, MI, USA, in 2002.

He is currently a Full Professor and the Eugene V. Polistuk Chair in Electromagnetic Design with the Department of Electrical and Computer Engineering, University of Toronto, Toronto, ON, Canada. His current research interests include numerical electromagnetics, with emphasis on high-order, multiscale computational methods, modeling under stochastic uncertainty, as well as applications of numerical methods to wireless channel modeling, wave-propagation in complex media and metamaterials, wireless power transfer, and electromagnetic compatibility/interference problems.

Dr. Sarris is the Chair of the MTT-S Technical Committee on Field Theory (MTT-15), the TPC Chair for the 2015 IEEE AP-S International Symposium on Antennas and Propagation and CNC/USNC Joint Meeting, and the TPC Vice Chair for the 2012 IEEE MTT-S International Microwave Symposium. He was a recipient of the IEEE MTT-S 2013 Outstanding Young Engineer Award. He served as an Associate Editor for the IEEE TRANSACTIONS ON MICROWAVE THEORY AND TECHNIQUES from 2009 to 2013 and the IEEE MICROWAVE AND WIRELESS COMPONENTS LETTERS from 2007 to 2009.

Jamesina J. Simpson (S'01–M'07–SM'12) received the B.S. and Ph.D. degrees in electrical engineering from Northwestern University, Evanston, IL, USA, in 2003 and 2007, respectively.

She is currently an Associate Professor with the Electrical and Computer Engineering Department, University of Utah, Salt Lake City, UT, USA. Her current research interests include the application of the full-vector Maxwell's equations finite-difference time-domain method to electromagnetic wave propagation spanning 15 orders of magnitude across the electromagnetic spectrum.

Dr. Simpson was a recipient of the 2010 National Science Foundation CAREER award, the 2012 Donald G. Dudley, Jr. Undergraduate Teaching Award of the IEEE AP-S, and the Santimay Basu Medal from URSI in 2017.